Lee-Vortex Formation in Free-Slip Stratified Flow over Ridges. Part I: Comparison of Weakly Nonlinear Inviscid Theory and Fully Nonlinear Viscous Simulations

C. C. EPIFANIO* AND D. R. DURRAN

Department of Atmospheric Sciences, University of Washington, Seattle, Washington

(Manuscript received 22 December 2000, in final form 17 August 2001)

ABSTRACT

The formation of lee wakes and vortices is explored in the context of stratified flow with uniform basic-state wind and stability past elongated free-slip ridges.

The theory of inviscid flow past a ridge of small nondimensional height ϵ is revisited using a weakly nonlinear semianalytic model to compute flow fields through $O(\epsilon^2)$. Consistent with previous work, the weakly nonlinear solutions show an $O(\epsilon^2)$ couplet of vertical vorticity above the lee slope of the appropriate sense to describe the observed circulation in lee vortices. Nonetheless, the actual $O(\epsilon^2)$ flow fields are found to be inconsistent with the developing lee-vortex structures observed in previous nonlinear numerical experiments. Lee-vortex formation must therefore depend significantly on finite-amplitude and/or dissipative effects not described by the weakly nonlinear inviscid model.

The weakly nonlinear results are compared to fully nonlinear numerical simulations of wake formation in viscous and thermally diffusive laminar flow. The nonlinear viscous simulations show a low-level hydraulic-jump-like structure in the lee of the obstacle, which is not predicted by the weakly nonlinear inviscid theory. A wake of decelerated fluid forms downstream of the jump with the surface flow in the wake reversing and lee vortices forming for sufficiently large ϵ. The vertical vorticity of the wake is concentrated along shear lines extending downstream from the lateral ends of the jump. In its qualitative features the low-level wake flow is surprisingly similar to previous shallow-water calculations.

1. Introduction

Significant attention has been devoted in the last decade to the study of lee-wake and vortex formation in stratified flow past isolated topographic obstacles. This effort has been motivated in large part by indications that the process of wake formation in stratified flow may be fundamentally different from that occurring in homogenous flows at high Reynolds number. In homogenous flow the vorticity of the wake is produced in the viscous boundary layer at the surface of the obstacle and shed into the interior of the fluid through the process of boundary-layer separation. That wakes in stratified flow might form in the absence of boundary-layer separation was first explored in a seminal study by Smolarkiewicz and Rotunno (1989, hereafter SR89). SR89 conducted a series of numerical simulations of stratified flow past topographic obstacles and found that realistic wakes and vortices formed even when a free-slip condition was applied at the obstacle surface. The free-slip condition eliminates the viscous boundary layer so that the simulated vortices of SR89 are clearly not due to boundary-layer separation. Similar indications have been provided by numerical modeling studies of observed wakes in the atmosphere; such studies show that neglecting or reducing surface friction often results in intensification rather than weakening of the simulated vortices (see discussion in Wilczak and Christian 1990). The idea that atmospheric wakes may form independent of boundary layer separation has stimulated several theoretical efforts attempting to explain the process of wake and vortex formation in free-slip stratified flows.

SR89 considered the idealized case of flow with uniform basic wind and stability past an axisymmetric topographic barrier. The authors proposed that the vertical vorticity of their simulated wakes and vortices derives from the baroclinic generation and tilting of vorticity in the three-dimensional gravity wave generated by the obstacle. To support their argument, SR89 considered a perturbation analysis of steady nondissipative flow past an obstacle of small nondimensional height $\epsilon = Nh_0/u_0$ (N is the base-state buoyancy frequency; u_0 is the base-state wind speed; and h_0 is the maximum height of the obstacle). Using the linear mountain wave solution of Smith (1980), SR89 showed that baroclinically

* Current affiliation: Department of Atmospheric Sciences, Texas A&M University, College Station, Texas.

Corresponding author address: Craig C. Epifanio; Department of Atmospheric Sciences, Texas A&M University, 3150 TAMU, College Station, TX 77843-3150.
E-mail: cepi@ariel.met.tamu.edu

generated $O(\epsilon)$ horizontal vorticity is tilted into the vertical by the $O(\epsilon)$ vertical velocity to produce a couplet of vertical vorticity over the lee slope at $O(\epsilon^2)$. The sign of this couplet was shown to be consistent with the observed circulations in the numerically simulated vortices. It was then assumed that this $O(\epsilon^2)$ couplet of vertical vorticity implies an $O(\epsilon^2)$ tendency to reverse the flow over the central part of the lee slope, thereby contributing to the formation of recirculating lee vortices.

SR89's basic argument involving baroclinic generation and tilting has been extended or modified in a number of subsequent studies (Crook et al. 1990, hereafter CCM90; Rotunno and Smolarkiewicz 1991, hereafter RS91; Davies-Jones 2000) to better account for nonlinear processes and time dependence. The need to consider highly nonlinear effects was particularly emphasized by CCM90. CCM90 considered numerical simulations of flow past an axisymmetric obstacle and noted that at small or moderate ϵ the fluid between the vortex centers over the lee slope is always accelerated. Only with the onset of wave breaking and a consequent increase in nonlinearity did the authors' simulations produce reversal of the lee-slope flow. This led CCM90 to question the ability of small-amplitude theory to account for the formation of lee vortices. Instead, CCM90 proposed that wave breaking leads to lee-vortex formation by inducing strong downward motion in the lee of the obstacle, thereby amplifying the tilting of baroclinically generated horizontal vorticity in the mountain wave. Note that in this respect the theories of SR89, CCM90, RS91, and Davies-Jones (2000) are all fundamentally similar: each attributes the vertical vorticity of the wake to the tilting of baroclinically generated horizontal vorticity by the vertical motion field in the lee of the obstacle.

A rather different description of wake and vortex formation based on shallow-water theory has been considered in some detail by Schär and Smith (1993, hereafter SS93). SS93 showed that in shallow-water flow, lee wakes and vortices may form as a result of vorticity and potential vorticity (PV) generation in hydraulic jumps. The restriction to shallow-water dynamics is intended as a first approximation to real atmospheric flows with distinct elevated inversions; indeed, the shallow-water model appears to provide a reasonable description of observed wakes in such flows (Smith and Grubišić 1993). Nonetheless, the implications of these results for more general flows without distinct inversions have remained uncertain. A particular limitation of the shallow-water approach is that in conventional shallow-water theory the flow in the infinitesimally thin region of the jump is left unspecified. As a result, the mechanisms of vorticity and PV generation are also left unspecified. The shallow-water analysis thus predicts the production of PV in the jump but provides no conceptual model to explain how air particles acquire vorticity and PV.

The present two-part study extends and, to some extent, synthesizes the results of SR89 and SS93 through the identification of fully finite-amplitude effects contributing to lee-vortex formation in free-slip stratified flows. Here, in Part I, we compare weakly nonlinear [i.e., valid through $O(\epsilon^2)$] semianalytic calculations and fully nonlinear numerical simulations in an effort to highlight the nonlinear processes leading to vortex development. The following section gives the experimental setup and briefly describes the numerical and semianalytic models. In section 3 the weakly nonlinear model is used to revisit the small-amplitude inviscid theory of SR89. It is shown that while the weakly nonlinear steady-state solution does reveal a couplet of vertical vorticity over the obstacle at $O(\epsilon^2)$, the associated $O(\epsilon^2)$ velocity fields do not suggest the low-level flow reversal characteristic of developing lee vortices. The small-amplitude results thus demonstrate that a tendency to reverse the flow over the lee slope cannot be deduced from the vertical vorticity alone—the horizontal vorticity and boundary conditions must also be considered.

Given that the weakly nonlinear inviscid model fails to predict recirculating vortices, the dynamics of lee vortex formation must be fundamentally dependent on either finite-amplitude processes or dissipative effects or both. Section 4 compares the small-amplitude results of section 3 with fully nonlinear numerical simulations. We consider the particular case of a moderate-Reynolds-number flow in which the viscosity and thermal diffusivity are large enough to prevent the development of small-scale turbulence; this model is adopted as the simplest context in which to analyze wake formation in stratified flow. Flow reversal and vortex formation in the nonlinear viscous simulations are found to be closely tied to the dynamics of a hydraulic-jump-like structure downstream of the obstacle. The resulting low-level flow is similar in many respects to the shallow-water calculations of SS93. Conclusions for Part I are given in section 5.

Part II of this study (Epifanio and Durran 2002) presents a detailed investigation into the mechanisms of vorticity and PV production in the nonlinear viscous wake. There it is shown that the vertical vorticity of the wake does in fact have its origins in the baroclinic generation and tilting mechanism of SR89. However, the vertical vorticity produced through tilting is relatively weak. The role of the hydraulic jump is then to amplify this vorticity through stretching as fluid particles pass through the jump, thereby producing the pronounced vertical vorticity anomalies of the wake.

2. Model descriptions

a. Experimental setup

We consider free-slip, nonrotating, compressible Boussinesq flow as described by

$$\frac{\partial u_i}{\partial t} + u_j\frac{\partial u_i}{\partial x_j} + \frac{\partial P}{\partial x_i} - \delta_{i3}b = -\frac{\partial T_{ij}}{\partial x_j}, \tag{1}$$

$$\frac{\partial b}{\partial t} + u_j\frac{\partial b}{\partial x_j} + N^2 w = -\frac{\partial B_j}{\partial x_j}, \quad \text{and} \tag{2}$$

$$\frac{\partial P}{\partial t} + c_s^2\frac{\partial u_j}{\partial x_j} = 0, \tag{3}$$

where $\mathbf{x} = (x_1, x_2, x_3) = (x, y, z)$ is the spatial position vector; $\mathbf{u} = (u, v, w)$ is the fluid velocity; P is the Boussinesq disturbance pressure and b the buoyancy; N is the basic-state buoyancy frequency; and c_s is the constant Boussinesq sound speed. The viscous stress and diffusive heat (or buoyancy) flux are given by

$$T_{ij} = -K_M\left(\frac{\partial u_i}{\partial x_j} + \frac{\partial u_j}{\partial x_i} - \frac{2}{3}\delta_{ij}\frac{\partial u_k}{\partial x_k}\right), \quad \text{and} \tag{4}$$

$$B_j = -K_H\frac{\partial b}{\partial x_j}, \tag{5}$$

where the kinematic viscosity K_M and the thermal diffusivity K_H are taken to be constants with Prandtl number $\mathrm{Pr} = K_M/K_H$ unity. We restrict attention to flows with constant N and uniform basic velocity $\mathbf{u}_0 = (u_0, 0, 0)$. The basic-state potential temperature variable is then $b_0(z) = N^2 z +$ constant.

The topography for all calculations takes the form of a smooth idealized ridge with long axis normal to the incident flow as defined by

$$h(x, y) = \begin{cases} \dfrac{h_0}{16}[1 + \cos(\pi r)]^4, & \text{if } r \le 1; \\ 0, & \text{otherwise,} \end{cases} \tag{6}$$

where

$$r^2 = \begin{cases} \left(\dfrac{x}{4a}\right)^2 + \left(\dfrac{|y| - (\beta - 1)a}{4a}\right)^2, & \text{if } |y| > (\beta - 1)a; \\ \left(\dfrac{x}{4a}\right)^2, & \text{otherwise.} \end{cases} \tag{7}$$

Here $\beta \ge 1$ is the horizontal aspect ratio defined as the ratio of y to x length scales for the topography. Note that for $\beta > 1$ a uniform height section appears in the ridge interior.

In all computations we set $N = 0.012\ \mathrm{s}^{-1}$, $u_0 = 8\ \mathrm{m\ s}^{-1}$, and $a = 10$ km. The resulting flow is nearly hydrostatic, with vertical aspect ratio $\delta = u_0/Na = 0.067$, and essentially incompressible, with Mach number $\mathrm{Ma} = u_0/c_s = 0.024$. We fix the aspect ratio at $\beta = 5$. With δ, Ma, and β specified, the set of control parameters reduces to the nondimensional mountain height (or nonlinearity parameter) $\epsilon = Nh_0/u_0$ and a Reynolds number describing the importance of viscosity and thermal diffusion. Here we define $\mathrm{Re} = u_0 h_0/K_M$ so as to be consistent with most previous laboratory studies (see, e.g., Baines 1995, p. 230); the numerically simulated $\epsilon = 1.8$ case considered in section 4 then has $\mathrm{Re} = 120$. [For comparison, Rotunno et al. (1999) define $\mathrm{Re} = u_0 a/K_M$, in which case $\mathrm{Re} = 1000$ for the simulated $\epsilon = 1.8$ case.] Both K_M and K_H are zero in the weakly nonlinear computations of section 3.

b. Weakly nonlinear semianalytic model

The linear and weakly nonlinear semianalytic models considered in section 3 represent the first and second terms in a perturbation solution of the inviscid, adiabatic, steady-state versions of (1)–(3) in the limit of small ϵ. The models are implemented using fast Fourier transforms (FFTs) on a large horizontally periodic domain. A brief description of the models including scale analysis is given in Epifanio and Durran (2001). Details of the weakly nonlinear model and verifications are provided in Epifanio (1999). Here we outline the semianalytic solution technique.

Under the assumption of small ϵ, the disturbance fields are expanded as

$$u - u_0 = u^{(1)} + u^{(2)} + \cdots, \qquad v = v^{(1)} + v^{(2)} + \cdots,$$

etc., where it is understood that $u^{(1)} \sim O(\epsilon)$, $u^{(2)} \sim O(\epsilon^2)$, and so forth. The expanded variables are substituted into the steady, inviscid, and adiabatic versions of (1)–(3) and terms of like power in ϵ are grouped. The resulting $O(\epsilon)$ system is equivalent to the linearized equations of Smith (1980), and solutions for the $O(\epsilon)$ flow fields and their spatial derivatives are obtained using the FFT method described there. The $O(\epsilon^2)$ system takes the form

$$u_0\frac{\partial u^{(2)}}{\partial x} + \frac{\partial P^{(2)}}{\partial x} = g_u, \tag{8}$$

$$u_0\frac{\partial v^{(2)}}{\partial x} + \frac{\partial P^{(2)}}{\partial y} = g_v, \tag{9}$$

$$u_0\frac{\partial w^{(2)}}{\partial x} + \frac{\partial P^{(2)}}{\partial z} - b^{(2)} = g_w, \tag{10}$$

$$u_0\frac{\partial b^{(2)}}{\partial x} + N^2 w^{(2)} = g_b, \quad \text{and} \tag{11}$$

$$\frac{\partial u^{(2)}}{\partial x} + \frac{\partial v^{(2)}}{\partial y} + \frac{\partial w^{(2)}}{\partial z} = 0, \tag{12}$$

with lower boundary condition

$$w^{(2)}(x, y, 0) = g_h. \tag{13}$$

The nonlinear forcing terms include the lower boundary correction

$$g_h = u^{(1)}(x, y, 0)\frac{\partial h}{\partial x} + v^{(1)}(x, y, 0)\frac{\partial h}{\partial y} - h\frac{\partial w^{(1)}}{\partial z}(x, y, 0), \quad (14)$$

and $O(\epsilon^2)$ advective terms of the form

$$g_u = -u^{(1)}\frac{\partial u^{(1)}}{\partial x} - v^{(1)}\frac{\partial u^{(1)}}{\partial y} - w^{(1)}\frac{\partial u^{(1)}}{\partial z} \quad (15)$$

(and similarly for g_v, g_w, g_b). The forcing functions are obtained as products of the $O(\epsilon)$ flow fields and derivatives on the numerical grid.

All disturbance quantities are assumed to vanish for $(x^2 + y^2)^{1/2} \to \infty$. Equations (8)–(12) then reduce to a single equation for $w^{(2)}$, which may be Fourier transformed in x and y to yield

$$\frac{d^2\tilde{w}^{(2)}}{dz^2} + m^2\tilde{w}^{(2)} = -\frac{\tilde{F}}{k^2u_0^2}, \quad (16)$$

where $\tilde{w}^{(2)}(k, l, z)$ denotes the horizontal Fourier transform of $w^{(2)}$. Here, m^2 is

$$m^2 = \left(\frac{N^2}{u_0^2} - k^2\right)\frac{k^2 + l^2}{k^2}, \quad (17)$$

and the nonlinear forcing is given by

$$\tilde{F}(k, l, z) = u_0k^2\frac{d\tilde{g}_u}{dz} + u_0kl\frac{d\tilde{g}_v}{dz} - (k^2 + l^2)\tilde{g}_b - iu_0k(k^2 + l^2)\tilde{g}_w. \quad (18)$$

Localized three-dimensional disturbances in a Boussinesq atmosphere decay in amplitude with height due to the horizontal dispersion of wave energy. As a result, the nonlinear forcing functions in (8)–(12) vanish in the limit $z \to \infty$. In practice the forcing functions must be neglected above some large but finite height z', and we thus set $\tilde{F}(z) = 0$ in (16) for $z > z'$. The height z' must be chosen sufficiently large that nonlinear interactions above z' have an insignificant impact on the solution below. For the $\beta = 5$ case discussed in section 3, it was found adequate to neglect the nonlinear forcings above $Nz'/u_0 = 20.3\pi$ (i.e., $z' \approx 10\lambda$, where $\lambda = 2\pi u_0/N$ is the vertical wavelength for two-dimensional hydrostatic waves). A radiation condition is then applied to ensure that all waves above z' have upward energy propagation.

For $u_0|k| < N$, the solution to (16) satisfying (13) and the radiation condition for $z > z'$ can be written in the form (see appendix for derivation)

$$\tilde{w}^{(2)}(k, l, z) = [\tilde{g}_h - C^-(z') + C^+(z)]e^{imz} + [C^-(z') - C^-(z)]e^{-imz}, \quad (19)$$

where

$$C^{\pm}(k, l, z) = \frac{i}{2m}\int_0^z \frac{\tilde{F}(k, l, \tau)}{k^2u_0^2}e^{\mp im\tau}\,d\tau, \quad (20)$$

and where the sign of m is chosen such that $m = (m^2)^{1/2}(k/|k|)$. For $u_0|k| > N$, an exponential decay condition is applied for $z > z'$ and solutions to (16) take the form of (19) and (20) with m replaced by $i\gamma$, where $\gamma = (-m^2)^{1/2}$. Given $\tilde{F}(k, l, z)$, the integrals in (20) (and those in the similar $u_0|k| > N$ case) are evaluated numerically for each k and l, and the results are used in (19) to obtain $\tilde{w}^{(2)}(k, l, z)$. Having solved for $\tilde{w}^{(2)}$, the remaining fields $\tilde{u}^{(2)}(k, l, z)$, $\tilde{v}^{(2)}(k, l, z)$, $\tilde{P}^{(2)}(k, l, z)$, and $\tilde{b}^{(2)}(k, l, z)$ are obtained through polarization relations derived from (8)–(12), as done for the $O(\epsilon)$ solution (see, e.g., Gill 1982, section 8.4). Polarization relations for all spatial gradients are obtained similarly. Inverse Fourier transformation at fixed z then gives the $O(\epsilon^2)$ flow fields and their spatial derivatives.

As noted by Smith (1980), the vertical wavenumber m approaches infinity as $k/l \to 0$. As a result, the integrals in (20) are difficult to evaluate numerically for small k/l due to rapid oscillations of the integrand in the vertical. Moreover, for small k/l the wavenumber m is a rapidly varying function of k, leading to rapid oscillations in the integrands of the Fourier inversion integrals [at both $O(\epsilon)$ and $O(\epsilon^2)$] as $k \to 0$ (D. J. Muraki 2000, personal communication). No attempt is made to explicitly deal with the singular behavior of the Fourier modes as $k/l \to 0$ in the present work.[1] To avoid the singularities we simply neglect modes for which $m > 7N/u_0$, effectively truncating the Fourier integrals at small k/l. Note that those modes for which k/l is small have negligible vertical group velocity, and their energy propagates primarily downstream as a result of advection by the basic flow (see Smith 1980). As such, the neglected modes are unlikely to contribute significantly to the solution directly over the obstacle, where the disturbance is dominated by modes with substantial vertical energy propagation. Indeed, the results of the weakly nonlinear semianalytic model have been verified by comparison to numerical estimates of the $O(\epsilon^2)$ flow fields obtained by subtracting the linear solution from high-precision nonlinear numerical simulations at small ϵ (Epifanio 1999; see also Fig. 3 of Epifanio and Durran 2001 for comparison of semianalytic and numerically simulated surface drags). The numerical and semianalytic predictions show reasonable agreement for all disturbance fields, especially directly over the obstacle. More accurate methods for dealing with the singularities in the Fourier computations will be considered in future work.

c. Numerical model

The numerical experiments in section 4 were conducted using a three-dimensional version of the non-

[1] To achieve sufficient accuracy in the $O(\epsilon^2)$ solutions, it was found necessary to use unusually large horizontal domain sizes. For example, the calculations of section 3 employed a horizontal domain of $270a \times 270a$. It is possible that the use of such large domains helps to resolve the rapid oscillations of the integrand in the fast Fourier inversion integrals by adding more modes at small k.

hydrostatic model described by Durran and Klemp (1983) as modified to solve the compressible-Boussinesq system (1)–(3). The solutions are computed in a terrain-following coordinate system with vertical coordinate

$$\gamma = \frac{z - h}{z_T - h} z_T, \tag{21}$$

where z_T is the depth of the model domain and $h(x, y)$ is the terrain height (Gal-Chen and Somerville 1975). The linear radiation condition of Klemp and Durran (1983) and Bougeault (1983) as modified for local evaluation by Durran (1999, section 8.3) is used at the upper boundary. A radiation condition with fixed-speed phase propagation is applied to normal velocities at the horizontal boundaries (Klemp and Lilly 1978). Approximate free-slip and thermal insulation conditions are applied by setting T_{13}, T_{23}, and B_3 to zero at the lower boundary under the assumption of topography with small slope.[2] The flow is initiated from rest by gradually accelerating the basic wind over the time interval $-4 \le u_0 t/a \le 0$.

To remove high-wavenumber numerical noise and maintain numerical stability we add weak fourth-derivative filters of the form

$$-\alpha\left(\left.\frac{\partial^4 u_i}{\partial x^4}\right|_\gamma + \left.\frac{\partial^4 u_i}{\partial y^4}\right|_\gamma\right), \qquad -\alpha\left(\left.\frac{\partial^4 b}{\partial x^4}\right|_\gamma + \left.\frac{\partial^4 b}{\partial y^4}\right|_\gamma\right) \tag{22}$$

to the right-hand sides of (1) and (2), respectively. The derivatives in (22) are taken at constant γ. The coefficient α is set so that the effective Reynolds number of the first of (22) is $u_0 a^3/\alpha = 10\,000$. The influence of the filters is then significantly weaker than the effects of viscosity and thermal conduction at the resolved scales of motion. However, the relative importance of the filters increases rapidly with decreasing scale. As a result, the filter terms are of the same order in magnitude as (but still smaller than) the viscous and thermal conduction terms in the hydraulic jump downstream of the obstacle (as briefly discussed in section 5 of Part II). A comparison simulation with $u_0 a^3/\alpha = 20\,000$ produced nearly identical results confirming that the filters have negligible impact on the dynamics of interest. However, the Lagrangian diagnostic computations in Part II were slightly degraded by short-wavelength noise when using the smaller value of α.

The horizontal extent of the model domain is given by $-12a \le x \le 18a$, $|y| \le (9 + \beta)a$ with $\Delta x = \Delta y = 0.125a$. The vertical grid spacing is $N\Delta z/u_0 = 0.031\pi$ at the lower boundary and increases geometrically with height with stretching factor 1.022 until reaching a maximum of $N\Delta z/u_0 = 0.119\pi$ near the upper boundary. The domain depth is $Nz_T/u_0 = 4.28\pi$. Both the vertical and horizontal extent of the domain are sufficient to minimize boundary sensitivities for the short time integrations considered here. The model employs a time-splitting technique to stably integrate terms associated with acoustic propagation on a small time step Δt_s while advancing the remaining terms on a larger step Δt. In all simulations $u_0\Delta t/a = 0.0056$ and $u_0\Delta t_s/a = 0.0056/3$.

[2] The true free-slip condition is $\mathbf{n} \times (\mathbf{T} \cdot \mathbf{n}) = 0$, where $\mathbf{T}$ is the viscous stress tensor (4) and $\mathbf{n}$ the unit normal to the boundary. Scale analysis of the true condition suggests that the approximate condition applied here is valid as long as $(h_0/a)^2 \ll 1$. In the present case $h_0/a = 0.12$ so that the approximation is warranted. Similar considerations apply to the thermal insulation condition $n_j B_j = 0$.

3. Weakly nonlinear inviscid theory

For steady and inviscid flow, the vorticity equation given by the curl of (1) is

$$(\mathbf{u} \cdot \boldsymbol{\nabla})\boldsymbol{\zeta} = (\boldsymbol{\zeta} \cdot \boldsymbol{\nabla})\mathbf{u} - \mathbf{k} \times \boldsymbol{\nabla} b, \tag{23}$$

where $\boldsymbol{\zeta} = (\xi, \eta, \zeta)$ is the vorticity, $\mathbf{k}$ is the vertical unit vector, and where the second term on the right is the Boussinesq approximation to the baroclinicity vector. In this section we use the weakly nonlinear semianalytic model to obtain solutions to (23) and the steady-state, nondissipative versions of (1)–(3) through $O(\epsilon^2)$. The basic state and topography are as given in section 2a.

a. Analysis

The $O(\epsilon)$ approximation to the vorticity equation (23) is given by

$$u_0 \frac{\partial \xi^{(1)}}{\partial x} = \frac{\partial b^{(1)}}{\partial y}, \qquad u_0 \frac{\partial \eta^{(1)}}{\partial x} = -\frac{\partial b^{(1)}}{\partial x},$$

$$u_0 \frac{\partial \zeta^{(1)}}{\partial x} = 0. \tag{24}$$

According to (24) the $O(\epsilon)$ wave field features baroclinically generated horizontal vorticity but is free of vertical vorticity. To obtain a first approximation to ζ we consider the $O(\epsilon^2)$ equation

$$u_0 \frac{\partial \zeta^{(2)}}{\partial x} = \xi^{(1)} \frac{\partial w^{(1)}}{\partial x} + \eta^{(1)} \frac{\partial w^{(1)}}{\partial y}, \tag{25}$$

which shows that vertical vorticity is produced at second order through tilting of the baroclinically produced horizontal vorticity. Equations (24), (25), and the $O(\epsilon)$ version of (2) may be combined to form the second-order PV equation

$$u_0 \frac{\partial}{\partial x}\left(\xi^{(1)} \frac{\partial b^{(1)}}{\partial x} + \eta^{(1)} \frac{\partial b^{(1)}}{\partial y} + N^2 \zeta^{(2)}\right) = 0, \tag{26}$$

where

$$Q^{(2)} = \xi^{(1)} \frac{\partial b^{(1)}}{\partial x} + \eta^{(1)} \frac{\partial b^{(1)}}{\partial y} + N^2 \zeta^{(2)} = 0 \tag{27}$$

is the $O(\epsilon^2)$ approximation to the potential vorticity $Q = \boldsymbol{\zeta} \cdot \boldsymbol{\nabla}(b_0 + b)$. Equation (27) expresses at $O(\epsilon^2)$ the constraint that, for inviscid and adiabatic flow with zero

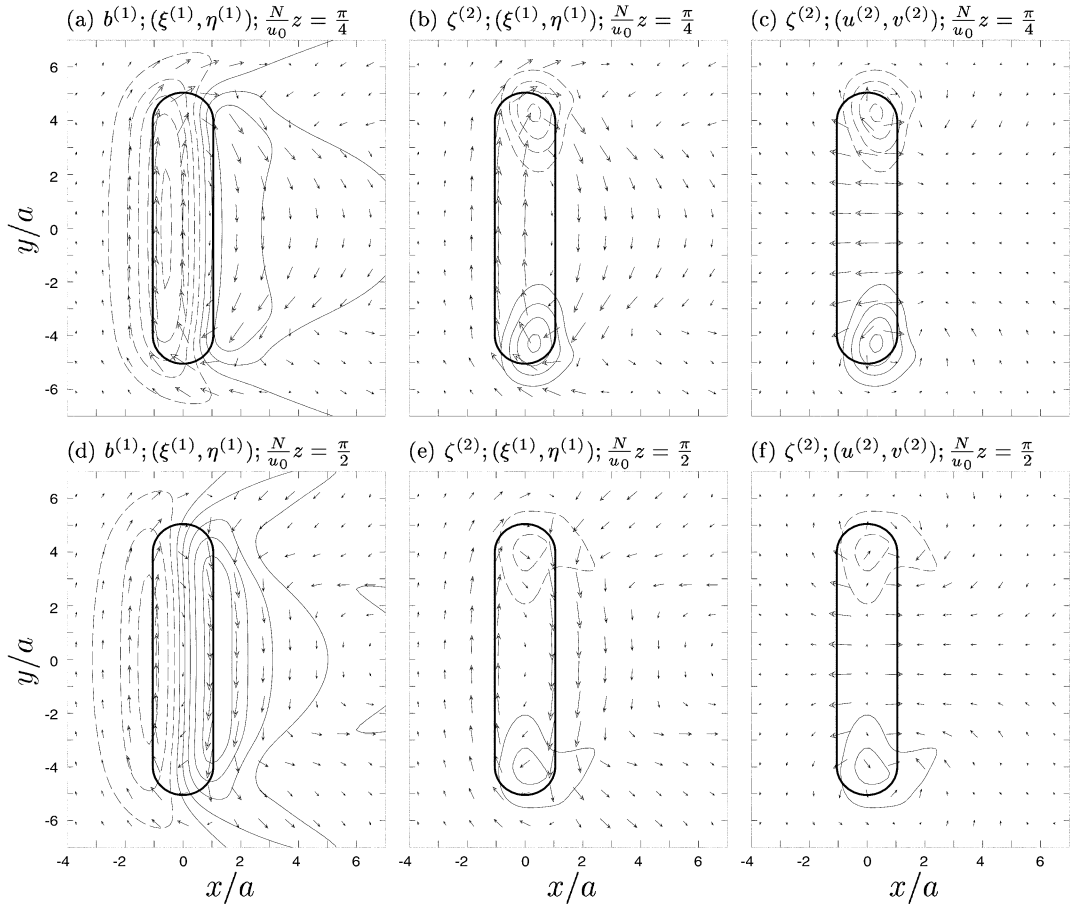

FIG. 1. Weakly nonlinear semianalytic solutions for flow of uniform wind and stability past an isolated ridge with $\beta = 5$. (a)–(c) Fields at height $Nz/u_0 = \pi/4$. (d)–(f) Fields at $Nz/u_0 = \pi/2$. The heavy line shows contour of half maximum ridge height. (a) and (d) Buoyancy $b^{(1)}/\epsilon N u_0$ (contour interval is 0.156, solid line is positive and dashed line is negative) and horizontal vorticity $(\xi^{(1)}, \eta^{(1)})/\epsilon N$ (maximum vector length is 0.583). (b) and (e) Vertical vorticity $\zeta^{(2)}/\epsilon^2\delta N$ (contour interval is 0.06) and $(\xi^{(1)}, \eta^{(1)})/\epsilon N$. (c) and (f) $\zeta^{(2)}/\epsilon^2\delta N$ and $O(\epsilon^2)$ flow $(u^{(2)}, v^{(2)})/\epsilon^2 u_0$ (maximum vector length is 0.4).

upstream PV, the vorticity must everywhere remain tangent to isentropic surfaces (i.e., surfaces of constant $b + b_0$).

SR89 use (27) to infer the $O(\epsilon^2)$ pattern of vertical vorticity associated with the $O(\epsilon)$ solution of Smith (1980). An equivalent computation is shown in Fig. 1 for a ridge with $\beta = 5$. Figures 1a and 1d show the buoyancy $b^{(1)}$ and horizontal vorticity $(\xi^{(1)}, \eta^{(1)})$ at $Nz/u_0 = \pi/4$ and $Nz/u_0 = \pi/2$, respectively. At both heights the vortex lines encircle the obstacle with positive $\eta^{(1)}$ upstream and negative $\eta^{(1)}$ downstream. At the lateral edges of the ridge the $O(\epsilon)$ vorticity vectors cross contours of $b^{(1)}$ implying that at $O(\epsilon^2)$ the vectors tilt upward on the right (viewed from upstream) and downward on the left so as to remain tangent to the sloping isentropic surface. The resulting $\zeta^{(2)}$ field as diagnosed from (27) is shown in Figs. 1b and 1e.

According to SR89 the $O(\epsilon^2)$ vertical vorticity shown in Figs. 1b and 1e implies negative $u^{(2)}$ in the region between the vortex centers and thus suggests a tendency to reverse the flow above the lee slope at large mountain heights. However, it is important to note that the vertical vorticity alone does not determine the second-order flow field. Figures 1c and 1f show the $O(\epsilon^2)$ horizontal velocity vectors $(u^{(2)}, v^{(2)})$ as computed by the weakly nonlinear semianalytic model at the heights considered in Figs. 1b and 1e. The figures clearly reveal a net circulation of the $O(\epsilon^2)$ flow around the centers of vertical vorticity. Nonetheless, note that $u^{(2)}$ is in fact positive above the lee slope. Figure 2b shows $u^{(2)}$ in cross section along the centerline $y = 0$ and reveals accelerated flow at low levels downstream of the crest where reversed flow typically occurs in numerically simulated lee vortices. The sum $u^{(1)} + u^{(2)}$ displayed for the case $\epsilon = 0.5$ in Fig. 2a similarly shows accelerated low-level flow downstream of the obstacle. The steady weakly nonlinear inviscid theory thus provides little indication of the leeside stagnation and flow reversal characteristic of lee vortices.

Consideration of the cross-stream vorticity η also suggests the inadequacy of the weakly nonlinear inviscid description. Scaling dependent and independent var-

iables as in Epifanio and Durran [2001; see also Smith and Grønås (1993)], the cross-stream vorticity may be written as

$$\eta = \epsilon N\left(\frac{\partial \hat{u}}{\partial \hat{z}} - \delta^2 \frac{\partial \hat{w}}{\partial \hat{x}}\right), \tag{28}$$

where hats denote nondimensional variables taken to be of order unity. For nearly hydrostatic disturbances (i.e., small δ) the cross-stream vorticity is given to a good approximation by $\partial u/\partial z$. Numerical simulations of nearly hydrostatic flow show that as the height of a topographic obstacle is increased, leeside stagnation and flow reversal at steady state occur first at the lower boundary (Rotunno et al. 1999, hereafter RGS99). The leeside flow also reverses first at the lower boundary in the initial value problem of flow started implusively from rest past a large topographic obstacle (RS91).[3] Reversal of the surface flow implies that developing vortices are characterized by a region of negative $u - u_0$ and positive $\eta \approx \partial u/\partial z$. However, this pattern is not seen above or downstream of the lee slope in the weakly nonlinear solution. Figures 2b and 2d show that in the lee of the obstacle, $\eta^{(2)} \approx \partial u^{(2)}/\partial z$ is positive only immediately above the lee slope where $u^{(2)}$ shows the flow to be accelerated. Indeed, farther aloft and farther downstream the negative values of $\eta^{(2)}$ suggest the steepening of the mountain wave rather than the formation of vortices at the surface. Comparison of Figs. 2a and 2c shows that similar arguments hold for $u^{(1)} + u^{(2)}$ and $\eta^{(1)} + \eta^{(2)}$.

b. Discussion

The weakly nonlinear description of lee vortices has been previously criticized by CCM90. CCM90 showed that in numerical simulations of flow past obstacles at small or moderate ϵ the net flow between the centers of vertical vorticity is actually accelerated. However, in their simulations the authors were unable to differentiate between $O(\epsilon)$ and $O(\epsilon^2)$ contributions to the net flow; the observed acceleration of the flow between the vortices was thus attributed to the known accelerative tendency at $O(\epsilon)$ (as derived by Smith 1980) while the contribution at $O(\epsilon^2)$ was left unspecified. As such, the comments of CCM90 do not explicitly address whether the second-order theory at least qualitatively predicts a tendency to form lee vortices at $O(\epsilon^2)$. Here we offer a more fundamental criticism of the small-amplitude analysis. The present results show that, even at $O(\epsilon^2)$, the weakly nonlinear inviscid theory does not predict flow fields that are consistent with the lee-vortex circulations observed in previous nonlinear numerical experiments. Finite-amplitude and/or dissipative effects must therefore play an essential role in producing even the qualitative sense of these observed circulations.

4. Nonlinear viscous flow morphology

In this section we consider the basic morphology of wakes and vortices in viscous and thermally diffusive laminar flow and compare the results to the weakly nonlinear calculations of the previous section.

a. The viscous model: General comments

As is typical in problems of geophysical interest, the most energetic scales of motion in atmospheric flow over orography are many orders of magnitude larger than the scales at which energy is removed by viscous dissipation. This broad range of relevant scales renders the true direct numerical simulation of such flows a practical impossibility for at least the foreseeable future. Indeed, most simulations of flow over three-dimensional orography to date have been limited to grid spacings that accurately resolve only the most energetic large-scale motions. The net effect of smaller-scale features is then represented through a subgrid-scale turbulence parameterization. Unfortunately, the degree to which these parameterizations realistically represent the subgrid-scale effects is often unclear; details of the flow that depend significantly on the parameterized turbulence must therefore be regarded with caution.

In the present context, the parameterization of subgrid-scale effects complicates the detailed analysis of vorticity and PV generation in orographic wakes. The turbulent diffusivities predicted by subgrid-scale parameterizations in orographic flows typically feature rather strong spatial gradients, which leads to significant vorticity generation by the associated turbulent stresses. It is presently uncertain whether this generation of vorticity can be considered realistic. Furthermore, simulations with parameterized turbulence often require significant numerical filtering to maintain numerical stability in regions where the parameterized dissipation is weak or inactive. This filtering is strictly unphysical but may account for a significant fraction of the net dissipation and associated PV generation in the flow (RGS99; Ólafsson and Bougeault 1996).

To avoid the uncertainties associated with turbulence

[3] CCM90 propose a distinctly different process of lee-vortex formation in the case where ϵ is increased gradually by decelerating the basic wind. The authors assert that, as u_0 is decreased, the flow reverses first aloft and that this region of flow reversal then descends to the surface in a time-dependent fashion. However, the evidence presented to support this conclusion is ambiguous. In their Fig. 7 an incipient region of decelerated surface flow is already evident in the lee of the obstacle even at the first time for which flow reversal occurs aloft ($t = 1000$ min); this decelerated surface flow is clearly distinct from the reversed flow in the breaking wave. Similarly, their Fig. 7c shows the flow to be nearly stagnant at the lower boundary—and perhaps even reversed as the zero contour is omitted—even though the reversed flow associated with wave breaking remains well aloft. It thus seems appropriate to conclude that there are separate regions of decelerated flow aloft and at the surface and that these regions in some sense merge as u_0 is decreased and the vertical scale contracts. We argue that it is the region of flow deceleration at the surface that is relevant to lee-vortex formation.

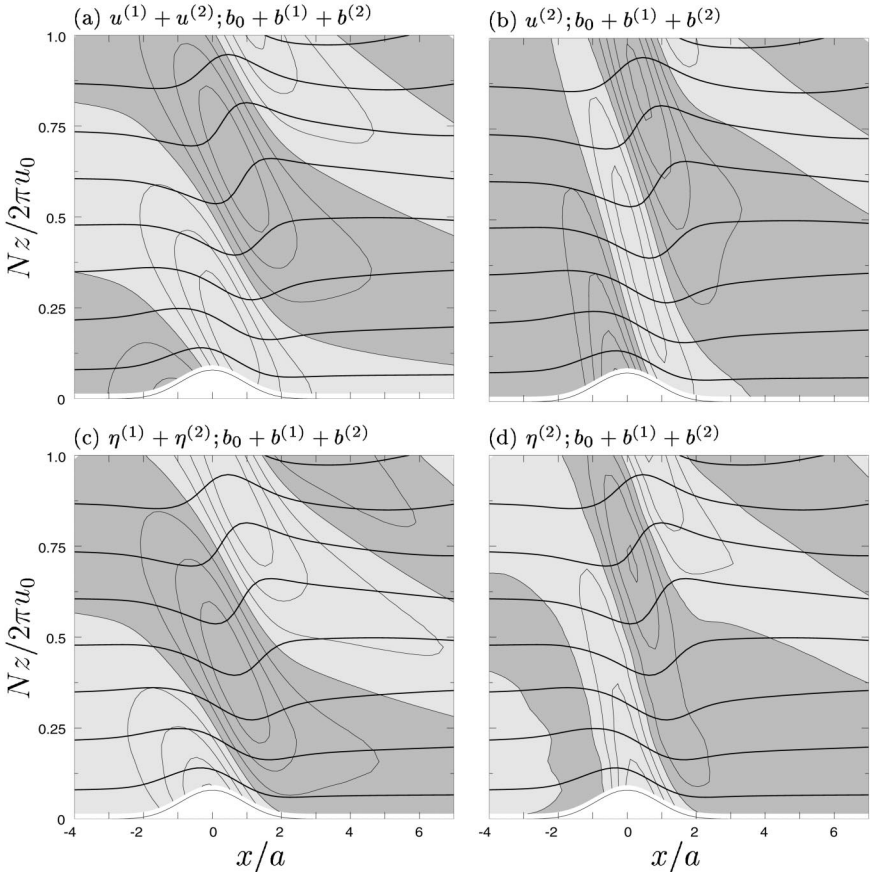

FIG. 2. Weakly nonlinear semianalytic solutions for flow of uniform wind and stability past an isolated ridge with $\beta = 5$ and $\epsilon = 0.5$. Fields shown along the line of symmetry $y = 0$. Dark lines in all panels are contours of potential temperature $(b_0 + b^{(1)} + b^{(2)})/Nu_0$ (contour interval is 0.833). (a) Disturbance speed $(u^{(1)} + u^{(2)})/\epsilon u_0$ (contour interval is 0.25; light shading is positive, dark shading is negative); (b) $O(\epsilon^2)$ correction $u^{(2)}/\epsilon^2 u_0$ (contour interval is 0.125); (c) cross-stream vorticity $(\eta^{(1)} + \eta^{(2)})/\epsilon N$ (contour interval is 0.25); and (d) $\eta^{(2)}/\epsilon^2 N$ (contour interval is 0.15).

parameterizations and numerical filtering, we instead opt to consider a moderate-Reynolds-number flow in which the onset of small-scale turbulence is suppressed by viscosity and thermal diffusion. Such a model has been considered previously by RGS99. While this laminar viscous case does not accurately represent real atmospheric flows, it does provide a complete and qualitatively realistic physical model in which to analyze wake and vortex formation. As illustrated in Part II, the developing vortex structures produced in the viscous flow are qualitatively very similar to those observed in identical simulations with parameterized turbulence. This suggests that the moderate-Reynolds-number case provides a useful starting point for understanding wake formation in more realistic high-Reynolds-number flows. Moreover, in the present simulations the Reynolds number is still sufficiently large that viscosity and thermal diffusion play secondary roles in the dynamics; qualitative comparison to the inviscid theory of section 3 is thus reasonable.

b. Numerical results

The figures in this section show results from fully nonlinear numerical simulations of viscous and thermally diffusive flow over free-slip ridges with $\beta = 5$ and $\epsilon = 1.5$, 1.8, and 2.2. The kinematic viscosity K_M is fixed so that the Reynolds number of the $\epsilon = 1.8$ case is $\mathrm{Re} = 120$. The remaining parameters are as given in section 2. The vertical cross sections are along the line of symmetry $y = 0$. The horizontal plots show fields on the terrain-following coordinate surface $N\gamma/u_0 = 0.351 \approx \pi/9$, which is the fourth scalar grid level from the lower boundary [see Durran and Klemp (1983) for discussion of the grid structure]. Figures 3 and 4 show fields from the $\epsilon = 1.8$ simulation at the first time for which lee-side flow stagnation occurs along $y = 0$ on the terrain-following analysis surface. (For the case considered, the flow along $y = 0$ reverses at the lower boundary one nondimensional time unit before the appearance of flow stagnation on the analysis surface.)

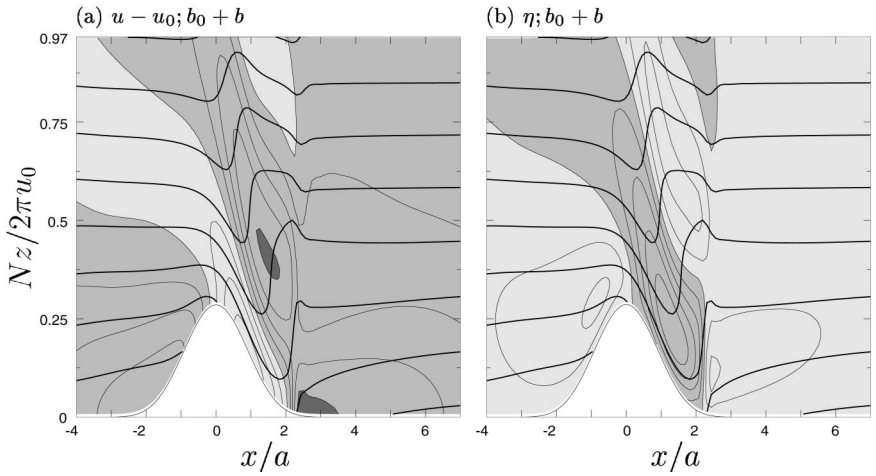

FIG. 3. Nonlinear numerical simulation of free-slip viscous flow with Re = 120 over an isolated ridge with $\beta = 5$ and $\epsilon = 1.8$. Fields are shown along the line of symmetry $y = 0$ at time $u_0 t/a = 7$. Dark lines are contours of potential temperature $(b_0 + b)/Nu_0$ (contour interval is 0.833). (a) Disturbance speed $(u - u_0)/\epsilon u_0$ [contour interval is 0.139, light shading is positive, dark shading is negative; values less than $-1/\epsilon$ (i.e., reversed flow) are indicated by darkest shading]; and (b) cross-stream vorticity $\eta/\epsilon N$ (contour interval is 0.15).

Figure 5 illustrates the time dependence of the flow for $\epsilon = 1.8$, while the $\epsilon = 1.5$ and $\epsilon = 2.2$ cases are considered in Fig. 6.

Figure 3a shows the streamwise disturbance speed $u - u_0$ and contours of constant $b_0 + b$ along the centerline of the ridge for the $\epsilon = 1.8$ case. The deflections of the isentropes suggest that the flow differs significantly in character from the weakly nonlinear case shown in Fig. 2. In the wave field above the obstacle the isentropes are steeply inclined creating a region of weak stability above the lee slope. Below the weak stability region is a stream of accelerated lee-slope flow coinciding with strongly depressed low-level isentropes. Downstream the isentropic surfaces abruptly return to nearly their upstream heights in a jump-like feature and the flow is decelerated. This lee-side flow structure is characteristic of waves with steeply inclined or overturning isentropes and has often been described for two-dimensional flow through analogy to nonlinear hydraulic theory (e.g., Baines 1995, section 5.11). In the following we consider the role of the leeside hydraulic jump in lee-wake and -vortex formation.

Figure 3b shows that the cross-stream vorticity η is negative in the region of accelerated lee-slope flow. Downstream of the jump the flow is decelerated and the cross-stream vorticity is positive. As discussed in section 3, lee wakes and vortices are characterized in cross section along $y = 0$ by a region of negative $u - u_0$ and positive $\eta \approx \partial u/\partial z$. Figure 3 suggests that the hydraulic jump plays an important role in establishing these conditions.

The horizontal structure of the jump for the $\epsilon = 1.8$ case is shown most clearly by the region of strong convergence in the horizontal wind (u, v) and strongly positive $\partial w/\partial z$ near $x/a = 2$ in Fig. 4d. Upstream and to the sides of the jump the flow is accelerated, while immediately downstream of the jump the wake flow is nearly stagnant. The jump is also outlined by the region of negative $\partial b/\partial x$ in Fig. 4e. As shown in Fig. 4e, the flow descending the lee slope encounters a positive x gradient of buoyancy upstream of the jump and thus develops negative cross-stream vorticity η [cf. (23)]. The hydraulic jump is characterized by strongly negative $\partial b/\partial x$, which reverses the cross-stream vorticity resulting in a region of positive η behind the jump. The resulting pattern of horizontal vorticity (ξ, η) is similar to the steady weakly nonlinear calculation upstream of the jump but differs downstream (compare Figs. 4a and 1a,d).

Comparison of Figs. 4b and 1b,e shows the vertical vorticity to be more strongly concentrated at the lateral edges of the wake in the nonlinear viscous solution than is predicted by the weakly nonlinear model. Note that in the nonlinear solution, the maxima of vertical vorticity are shifted downstream of the obstacle and are connected by horizontal vorticity vectors that run directly across the wake from negative to positive y. In cross section in the y–z plane (not shown), the vortex lines connecting the vorticity centers arch up and over the wake as shown by Schär and Durran (1997, their Fig. 12) and RGS99 (their Fig. 4c). This structure of the vortex lines is consistent with positive η in the wake region as diagnosed above and represents an important discrepancy from the weakly nonlinear inviscid theory. Figure 4f shows that the vertical vorticity maxima are located slightly downstream of the lateral edges of the jump (as defined by the shaded area of strongly negative $\partial b/\partial x$). The regions of strong vertical vorticity extending downstream from the jump define the shear lines between the decelerated wake flow and the accelerated flow outside the wake. Note that in contrast to the weak-

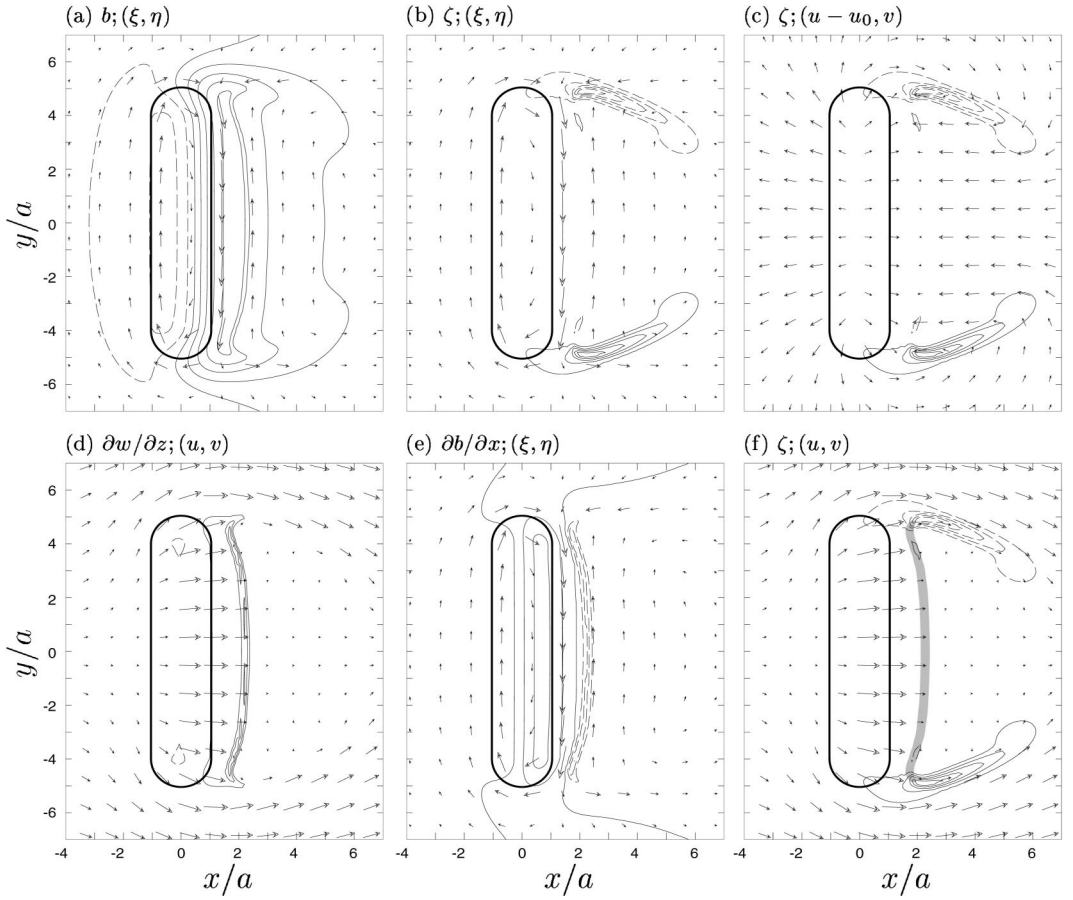

FIG. 4. Nonlinear numerical simulation of free-slip viscous flow with Re = 120 over an isolated ridge with $\beta = 5$ and $\epsilon = 1.8$. Fields shown on the terrain-following coordinate surface $N\gamma/u_0 \approx \pi/9$ at time $u_0t/a = 7$. Here and in the following, solid lines indicate positive values and dashed lines negative: (a) buoyancy $b/\epsilon N u_0$ (contour interval is 0.174) and horizontal vorticity $(\xi, \eta)/\epsilon N$ (maximum vector length is 0.46); (b) vertical vorticity $\zeta/\epsilon^2\delta N$ (contour interval is 0.21) and $(\xi, \eta)/\epsilon N$; (c) $\zeta/\epsilon^2\delta N$ and disturbance horizontal velocity $(u - u_0, v)/\epsilon u_0$ (maximum vector length is 1.04); (d) $(1/\epsilon\delta N)\partial w/\partial z$ (contour interval is 0.69) and horizontal velocity $(u, v)/u_0$ (maximum vector length is 1.875); (e) $(a/\epsilon N u_0)\partial b/\partial x$ (contour interval is 0.579) and $(\xi, \eta)/\epsilon N$; (f) $\zeta/\epsilon^2\delta N$, $(u, v)/u_0$, and $(a/\epsilon N u_0)\partial b/\partial x$ (shading indicates values less than -0.579).

ly nonlinear case the disturbance flow $(u - u_0, v)$ clearly forms closed circulations around the centers of vertical vorticity (compare Figs. 4c and 1c,f).

The time dependence of wake and vortex formation in the $\epsilon = 1.8$ case is shown in Fig. 5. At time $u_0t/a = 0$, the strong negative x gradient of buoyancy characteristic of the jump has formed[4] in the lee of the obstacle, and the flow has begun to curl around the lateral edges of the jump. Note that even at this early time the maxima of vertical vorticity are located downstream of the jump and are connected by horizontal vorticity vectors (ξ, η) running behind the jump from negative to positive y (Fig. 5d). At $u_0t/a = 5$, the fluid immediately behind the jump is nearly stagnant and the flow past the lateral edges of the jump is accelerated. The vertical vorticity anomalies defining the shear lines have begun to extend downstream. At $u_0t/a = 10$ the flow behind the jump is weakly reversed, indicating the onset of the recirculating vortex flow. The region of decelerated wake flow has grown in horizontal extent and the vorticity anomalies continue to extend downstream. Note that both the flow reversal behind the jump as well as the concentrated anomalies of vertical vorticity at the edges of the wake in Fig. 5c are suprisingly suggestive of the shallow-water calculations of SS93 (see their Fig. 6).

The ϵ dependence of the wake at fixed viscosity is considered in Fig. 6. Note that the $\epsilon = 1.5$ case shown in Figs. 6a and 6b is below the threshold ϵ at which flow reversal occurs in the wake. Nonetheless, the basic features of the flow are similar to those seen in Figs. 3 and 4. Over the lee slope the isentropes in Fig. 6a are displaced strongly downward and downstream there is a recovery zone in which the isentropes nearly regain

[4] Recall that the disturbance is initiated by accelerating the basic flow over the time interval $-4 \le u_0t/a \le 0$.

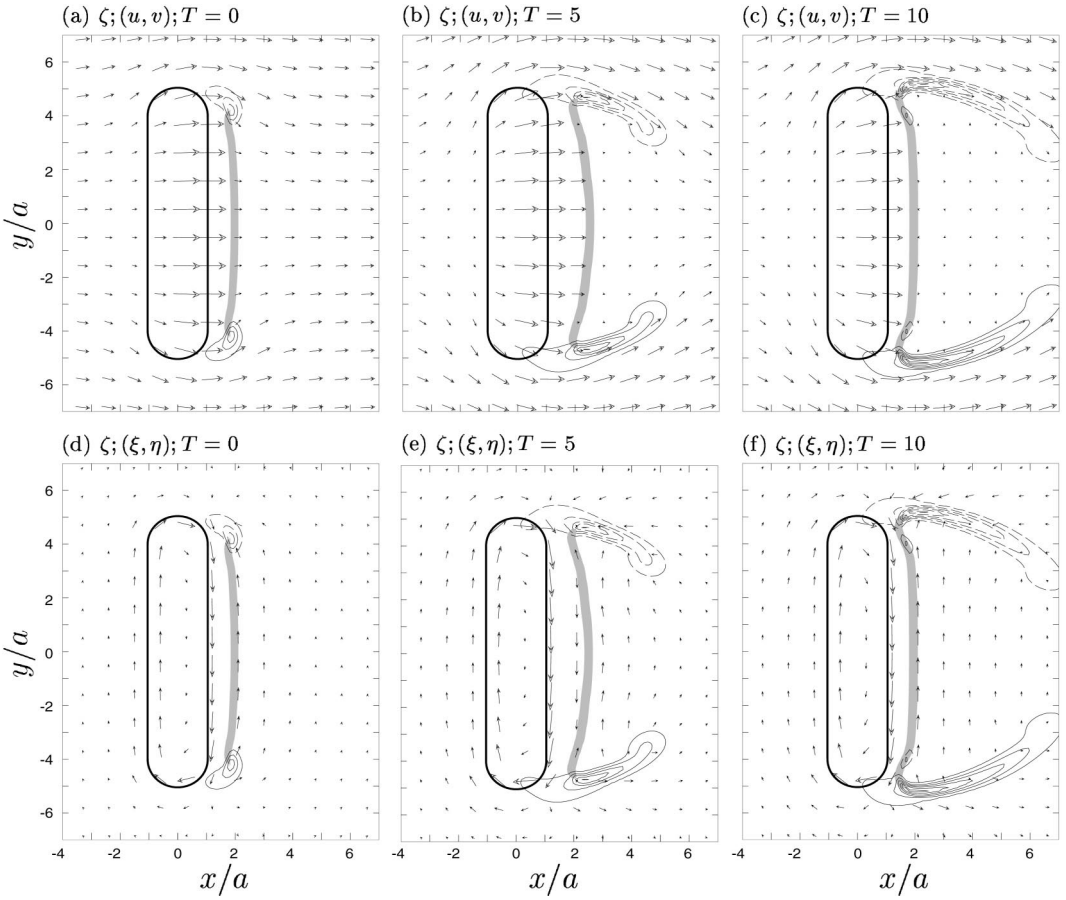

FIG. 5. Time dependence of vortex formation in free-slip viscous flow over an isolated ridge. Shading in all panels indicates values of $(a/\epsilon N u_0)\partial b/\partial x$ less than -0.579. (a)–(c) Vertical vorticity $\zeta/\epsilon^2\delta N$ (contour interval is 0.21) and horizontal velocity $(u, v)/u_0$ at times $u_0 t/a = 0$, 5, and 10, respectively. (d)–(f) $\zeta/\epsilon^2\delta N$ and horizontal vorticity $(\xi, \eta)/\epsilon N$ (maximum vector length is 0.46) at times $u_0 t/a = 0$, 5, and 10.

their upstream heights. Behind this recovery zone the flow is decelerated and $\partial u/\partial z$ is positive. In plan view the vertical vorticity is again found to be concentrated along shear lines at the lateral edges of the wake. As in Fig. 4f the maxima in $|\zeta|$ occur just slightly downstream of the region of strongly negative $\partial b/\partial x$ in the recovery zone.

As ϵ is increased from 1.5 to 1.8, the recovery zone in Fig. 6a steepens into the jumplike structure shown in Fig. 3. Note that the steepening of the isentropes is most pronounced at low levels. Further increases in ϵ cause further steepening of the jump until at $\epsilon = 2.2$ the jump is only marginally resolved on the numerical mesh (Fig. 6c). At larger ϵ significant numerical artifacts appear in the vicinity of the jump due to the inability to resolve the steep gradients. It is likely that in a higher-resolution simulation the jump would overturn and become turbulent at this stage. Note that as ϵ is increased, the production of vertical vorticity increases rapidly (note the $\epsilon^2\delta N$ scaling for ζ in the figures) and the recirculating vortices form more quickly. In the $\epsilon = 2.2$ case shown in Fig. 6d, the recirculating vortex flow is already well-established at time $u_0 t/a = 7$ (cf. Fig. 4f).

5. Summary and discussion

This study has explored lee-vortex formation in free-slip stratified flow over elongated ridges. Weakly nonlinear inviscid calculations and fully nonlinear viscous simulations were compared in an effort to identify processes leading to vortex development. As predicted by SR89, the weakly nonlinear solutions reveal an $O(\epsilon^2)$ couplet of vertical vorticity over the lee slope produced through the tilting of baroclinically generated horizontal vorticity. However, the associated horizontal velocity field $(u^{(2)}, v^{(2)})$ shows no tendency to reverse the lee-slope flow between the vortex centers. Furthermore, in regions where $u^{(2)}$ is negative, the cross-stream vorticity $\eta^{(2)} \approx \partial u^{(2)}/\partial z$ is of the wrong sense to describe vortex development at the surface. These results suggest that the mechanism of vorticity tilting in nondissipative flow as described by weakly nonlinear theory provides an

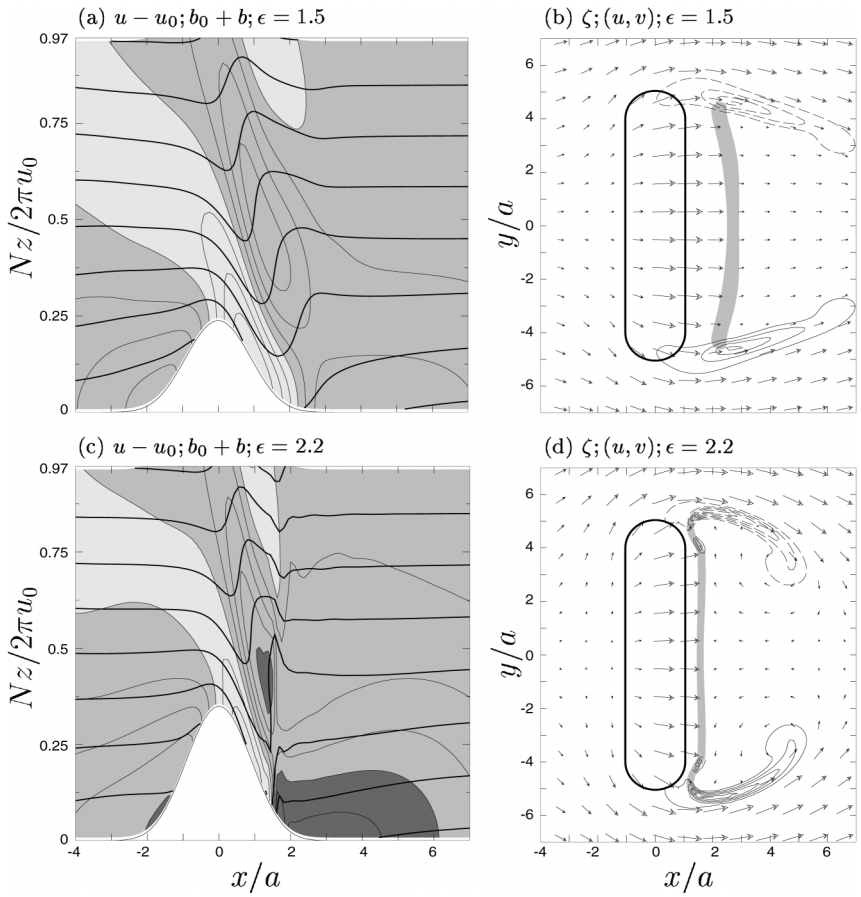

FIG. 6. Basic wake features for $\epsilon = 1.5$ and $\epsilon = 2.2$. (a) and (b) Fields for $\epsilon = 1.5$; (c) and (d) $\epsilon = 2.2$. All fields shown at time $u_0t/a = 7$. Both (a) and (c) have disturbance speed $(u - u_0)/u_0$ (contour interval is 0.25; light shading is positive; dark shading is negative; darkest shading indicates reversed flow) and potential temperature $(b_0 + b)/Nu_0$ (contour interval is 0.833). (b) and (d) As in Fig. 4f, except shading in (b) indicates values of $(a/\epsilon Nu_0)\partial b/\partial x$ less than -0.35.

inadequate description of lee-vortex formation. A more complete description then requires the consideration of additional finite-amplitude and/or dissipative effects.

The weakly nonlinear results were compared to a fully nonlinear numerical simulation of laminar moderate-Reynolds-number (Re = 120) flow past an obstacle of medium height ($\epsilon = 1.8$). Wake formation in the laminar viscous case is found to be closely tied to a low-level hydraulic-jump-like feature that is not predicted by the weakly nonlinear calculations. Upstream of the jump the lee-slope flow is accelerated and is similar in character to supercritical hydraulic flow. Upon crossing the jump the flow deepens and decelerates and a wake of nearly stagnant fluid forms downstream of the jump. The vertical vorticity of the wake is concentrated into narrow bands extending downstream from the lateral ends of the jump. At later times the flow behind the jump reverses and recirculating vortices form. The low-level flow is then qualitatively very similar to the shallow-water calculations of SS93 (their Fig. 6). As ϵ is increased the hydraulic jump becomes steeper and recirculating vortices form more rapidly. For $\epsilon > 2.2$, the jump is no longer resolved by the numerical mesh and the flow would likely become turbulent if simulated at higher resolution.

In the present simulations the hydraulic-like nature of the leeside flow is highlighted through the consideration of a long, uniform-height ridge. Nonetheless, it can be argued in retrospect that hydraulic-jump-like features are also evident in previous numerical studies of wakes in flow past circular (Fig. 3 of Schär and Durran 1997; Fig. 2 of RS91) and elliptical (Fig. 2 of Ólafsson and Bougeault 1996) obstacles, at least for moderate obstacle heights. For large obstacles ($\epsilon \gtrsim 3$, say), the jumplike features in the centerline plane are typically weak or absent at steady state but may nonetheless be prominent during the rapid early evolution of the vortices (Fig. 1 of RS91). Even at steady state jumps may occur on the flanks of large obstacles rather than in the centerline plane (Ólafsson and Bougeault 1996).

The importance of hydraulic jumps in lee-wake formation has previously been suggested for shallow-water

flow (SS93) and for the analogous case of stratified flow with a distinct elevated inversion (Smith and Grubišić 1993). The present results show that the formation of lee wakes and vortices may be closely tied to the dynamics of hydraulic-jump-like features even in flow with uniform basic wind and stability. In terms of vorticity, the negative x gradient of buoyancy across the jump directly contributes to the generation of positive $\eta \approx \partial u/\partial z$ in the wake and thereby promotes the reversal of the surface flow. Similarly, the pronounced anomalies of vertical vorticity extending downstream from the lateral ends of the jump suggest that the jump is in some way responsible for creating the vertical vorticity of the wake. However, the mechanism of vertical vorticity production cannot be determined from the qualitative analysis given here. In Part II it is shown that the wake vertical vorticity actually originates through baroclinic generation and tilting in the mountain wave upstream of the jump, much as described by SR89. This vorticity is then strongly amplified by vortex stretching as fluid particles pass through the jump. To obtain these results we use a new method of vorticity diagnosis developed in Part II.

Acknowledgments. The authors acknowledge many stimulating discussions with Rich Rotunno. This research was sponsored by NSF Grants ATM-9530662 and ATM-9817728.

APPENDIX

Solution of the Vertical Structure Equation

The solution to (16) with (13) can be written in the form

$$\tilde{w}^{(2)}(z) = \tilde{g}_h e^{imz} - \int_0^{z'} \frac{\tilde{F}(\tau)}{k^2 u_0^2} G(z, \tau)\, d\tau, \qquad \text{(A1)}$$

where, as in section 2b, we have assumed that $\tilde{F}(z) = 0$ for $z > z'$. Here, $G(z, \tau)$ is the Green's function satisfying

$$\frac{d^2G}{dz^2} + m^2 G = \delta(z - \tau), \qquad \text{(A2a)}$$

with boundary conditions

$$G(z, \tau) \propto e^{imz} \quad \text{for } z > \tau, \quad \text{and} \qquad \text{(A2b)}$$

$$G(0, \tau) = 0. \qquad \text{(A2c)}$$

The condition (A2b) ensures upward energy propagation for $z > z'$, while (A2c) guarantees that the integral term in (A1) vanishes at $z = 0$. The solution to (A2) is

$$G(z, \tau) = \begin{cases} \dfrac{i}{2m}(e^{im\tau} - e^{-im\tau})e^{imz}, & \text{for } z > \tau; \\ \dfrac{i}{2m} e^{im\tau}(e^{imz} - e^{-imz}), & \text{for } z < \tau. \end{cases} \qquad \text{(A3)}$$

Substituting (A3) into (A1), breaking the integral into subintegrals over $[0, z]$ and $[z, z']$, and then rearranging terms yields (19).

REFERENCES

Baines, P. G., 1995: *Topographic Effects in Stratified Flows.* Cambridge University Press, 482 pp.

Bougeault, P., 1983: A non-reflective upper boundary condition for limited-height hydrostatic models. *Mon. Wea. Rev.*, **111,** 420–429.

Crook, A. N., T. L. Clark, and M. W. Moncrieff, 1990: The Denver cyclone: Formation in low Froude number flow. *J. Atmos. Sci.*, **47,** 2725–2742.

Davies-Jones, R., 2000: A Lagrangian model for baroclinic genesis of mesoscale vortices. Part I: Theory. *J. Atmos. Sci.*, **57,** 715–736.

Durran, D. R., 1999: *Numerical Methods for Wave Equations in Geophysical Fluid Dynamics.* Springer-Verlag, 460 pp.

——, and J. B. Klemp, 1983: A compressible model for the simulation of moist mountain waves. *Mon. Wea. Rev.*, **111,** 2341–2361.

Epifanio, C. C., 1999: High-drag states and lee vortices in stratified flow over topography. Ph.D. dissertation, University of Washington, 97 pp.

——, and D. R. Durran, 2001: Three-dimensional effects in high-drag-state flows over long ridges. *J. Atmos. Sci.*, **58,** 1051–1065.

——, and ——, 2002: Lee-vortex formation in free-slip stratified flow over ridges. Part II: Mechanisms of vorticity and PV production in nonlinear viscous wakes. *J. Atmos. Sci.*, 1166–1181.

Gal-Chen, T., and R. Somerville, 1975: On the use of a coordinate transformation for the solution of the Navier–Stokes equations. *J. Comput. Phys.*, **17,** 209–228.

Gill, A. E., 1982: *Atmosphere–Ocean Dynamics.* Academic Press, 662 pp.

Klemp, J. B., and D. K. Lilly, 1978: Numerical simulation of hydrostatic mountain waves. *J. Atmos. Sci.*, **35,** 78–107.

——, and D. R. Durran, 1983: An upper boundary condition permitting internal gravity wave radiation in numerical mesoscale models. *Mon. Wea. Rev.*, **111,** 430–444.

Ólafsson, H., and P. Bougeault, 1996: Nonlinear flow past an elliptic mountain ridge. *J. Atmos. Sci.*, **53,** 2465–2489.

Rotunno, R., and P. K. Smolarkiewicz, 1991: Further results on lee vortices in low-Froude-number flow. *J. Atmos. Sci.*, **48,** 2204–2211.

——, V. Grubišić, and P. K. Smolarkiewicz, 1999: Vorticity and potential vorticity in mountain wakes. *J. Atmos. Sci.*, **56,** 2796–2810.

Schär, C., and R. B. Smith, 1993: Shallow-water flow past isolated topography. Part I: Vorticity production and wake formation. *J. Atmos. Sci.*, **50,** 1373–1400.

——, and D. R. Durran, 1997: Vortex formation and vortex shedding in continously stratified flows past isolated topography. *J. Atmos. Sci.*, **54,** 534–554.

Smith, R. B., 1980: Linear theory of stratified hydrostatic flow past an isolated mountain. *Tellus*, **32,** 348–364.

——, and S. Grønås, 1993: Stagnation points and bifurcation in 3-D mountain airflow. *Tellus*, **45A,** 28–43.

——, and V. Grubišić, 1993: Aerial observations of Hawaii's wake. *J. Atmos. Sci.*, **50,** 3728–3750.

Smolarkiewicz, P. K., and R. Rotunno, 1989: Low Froude number flow past three-dimensional obstacles. Part I: Baroclinically generated lee vortices. *J. Atmos. Sci.*, **46,** 1154–1164.

Wilczak, J. M., and T. W. Christian, 1990: Case study of an orographically induced mesoscale vortex (Denver cyclone). *Mon. Wea. Rev.*, **118,** 1082–1102.